All-optical observation on
activity-dependent nanoscale dynamics of myelinated axons

Junhwan Kwon[1,2,#], Sungho Lee[3,4,#], Yongjae Jo[2], Myunghwan Choi[3,4,*]

[1]Department of Biomedical Engineering, Sungkyunkwan University, Suwon, Republic of Korea. [2]Center for Neuroscience Imaging Research, Institute for Basic Science, Suwon, Republic of Korea. [3]School of Biological Sciences, Seoul National University, Seoul, Republic of Korea. [4]The Institute of Molecular Biology and Genetics, Seoul National University, Seoul, Republic of Korea. [#]These authors contributed equally to this work.

* Correspondence to:
M. Mark Choi, Ph.D.
Associate Professor
School of Biological Sciences, Seoul National University
Address: 1 Gwanak-ro, Gwanak-gu, Seoul 08826
Tel: +82-2-880-4420
Email: choim@snu.ac.kr

1   **ABSTRACT**

2

3   In the mammalian brain, rapid conduction of neural information is supported by the myelin, whose

4   functional efficacy shows steep dependence on its nanoscale cytoarchitecture. Although previous in

5   vitro studies suggested that neural activity accompanies nanometer-scale cellular deformations, it has

6   remained unexplored whether neural activity can dynamically remodel the myelinated axon due to the

7   technical challenge in observing its nanostructural dynamics in living tissues. To this end, we

8   introduced a novel all-optical approach combining a nanoscale dynamic readout based on spectral

9   interferometry and optogenetic control of neural excitation on a living brain slice preparation. In

10   response to optogenetically evoked neuronal burst firing, the myelinated axons exhibited progressive

11   and reversible spectral redshifts, corresponding to the transient swelling at a subnanometer scale. We

12   further revealed that the activity-dependent nanostructural dynamics was localized to the paranode. In

13   summary, our novel all-optical studies substantiate that myelinated axon exhibits activity-dependent

14   nanoscale swelling, which potentially serves to dynamically tune the transmission speed of neural

15   information.

16

17

18

19

20   **RESEARCH SUMMARIES**

21

22   As neural activity involves rapid ion flux across the cell membrane, researchers have long been

23   tried to detect the accompanying nanoscale morphological dynamics. However, measuring the

24   activity-dependent nanostructural dynamics in the living mammalian brain has been an enigma

25   due to the technical limitations. By combining excitatory optogenetics and *in situ* nanoscale

26   metrology based on spectral interference, we demonstrate the first direct observation that the

27   mammalian axons exhibit transient activity-dependent swelling at subnanometer-scale.

28

INTRODUCTION

As neurons function by millisecond-scale ion flux across the cell membrane, neural activity has long been thought to accompany measurable morphological changes[1–3]. Since the late 1970s, several groups have reported nanometer-scale swelling in the giant axons of invertebrate species (crayfish and squid) by Michelson interferometry[4] and mechanoelectrical measurement[5]. Later studies in mammalian cultured neurons by dark-field microscopy and full-field interferometry revealed the subnanometer-scale morphological dynamics dependent on electrical potential across the neuronal cell membrane[4–8].

Yet, it is remained as an enigma to what extent neural activity dynamically remodel the axons in living mammalian brains, which are often ensheathed by the insulating layer - myelin. Myelin is a highly compacted subcellular structure of the oligodendrocyte, composed of multi-layered lipid membranes and intervening aqueous mediums. This highly-organized thin-film cytoarchitecture supports rapid and energy-efficient conduction of neural information in a small form factor, enabling formation of highly integrated circuit of the mammalian brains[9,10]. Considering that the function of myelin has steep dependence on its thin-film structure, the structural dynamics of myelinated axons, even at subnanometer-scale, can have critical impact on neural circuit functions[11].

Investigating the nanostructural dynamics of myelinated axons in living mammalian brains is technically challenging. The current gold-standard on nanoscale imaging of myelinated axons is electron microscopy, which is hardly adoptable to the living biological samples[12–14]. Super-resolution techniques are a promising alternative for living biological samples but subnanometer-scale precision has yet been attained in the mammalian axons due to high optical aberrations of the lipid-rich myelin layers[15–17]. Thus, most studies so far focused on long-term dynamics of relatively large morphological changes involving cell proliferation and differentiation[11–13,18].

Several years ago, we developed a spectral interferometric technique, named SpeRe, which offers the nanoscale readout of the thin-film cytoarchitecture of the myelinated axons in vivo[19]. Here, we combined the SpeRe's nanoscale readout with optogenetic manipulation of neural activity to unveil the neural activity dependent nanostructural dynamics of myelinated axons in a living brain tissue. Our novel all-optical approach revealed that the myelinated axons exhibit subnanometer-scale swelling in response to neuronal burst firing, and that the swelling dynamics is cumulative and reversible in second-scale.

62 **RESULTS**

63

64 **System for all-optical investigation**

65 To observe morphological dynamics of functionally active myelinated axons at nanoscale, we

66 introduced a novel all-optical neurophysiology approach (**Fig. 1a,b**). For manipulating neural

67 excitation with minimal mechanical perturbation, we introduced red-shifted excitatory optogenetic

68 protein (ChrimsonR) into cortical excitatory neurons. Neuronal excitation was timely triggered by epi-

69 illuminated fiber-coupled LED at 633 nm on an acute brain slice, and was confirmed by GCaMP-

70 mediated functional calcium imaging on the targeted neurons by two-photon microscopy[20]. For

71 recording nanostructural dynamics of myelinated axons, we incorporated spectral reflectometry

72 (SpeRe), that captures broadband reflectance spectrums at the geometric center of the axons and

73 decodes the physical size of the multilayered thin-films (i.e., diameter of the myelinated axons) by

74 decoding the spectrums. To assist the pinpointing of the geometric centers, we additionally introduced

75 spectral confocal reflectance imaging (SCoRe)[21], which provides a volumetric image of reflected light

76 corresponding to the centerlines of myelinated axons.

77 The overall procedure for nanostructural readout begins with acquisition of a volumetric

78 reflectance image from a fresh brain slice by SCoRe (**Fig. 1c**). From the volumetric SCoRe image, the

79 position of maximum intensity for each cross-section is localized, resulting in the geometric centerline

80 along the fibrous structure. The broadband reflectance spectrum is subsequently acquired over time

81 at the center positions, and the structural dynamics is decoded from the acquired spectrums (SpeRe).

82 For decoding of nanostructural dynamics, we performed numerical optic simulation on the

83 myelinated axons and obtained quantitative relationship between the reflectance spectrum and the

84 nanoscale cytoarchitecture. Briefly, interaction of light waves at the subcellular layers of myelinated

85 axons were described by the thin-film matrix theory, and distribution of light waves at the focus was

86 formulated by the vector diffraction theory. As the morphological dynamics was observed exclusively

87 at the paranode of myelinated axons in our following experiments, we set the simulation parameters

88 including physical size and refractive index for each subcellular layer based on the paranodal region

89 (**Supplementary Table 1**).

90 The resulting simulation database showed that the swelling of myelinated axons ($\Delta D > 0$) leads

91 to negative phase-shift in wavenumber domain ($\Delta v < 0$) with linear relationship (**Supplementary Fig.**

92 **1**). Thus, we decided to use the relative phase-shift (Δv) as a reliable metric to quantify the dynamic

93 swelling of myelinated axons (i.e., phase detection method[22–24]). To detect subnanometer-scale

94 morphological dynamics, we used the grating of 600 lines·mm^{-1} and slit size of 10 μm, resulting in

95 spectral resolution of ~0.13 nm.

96

97 **Validation of subnanometer-scale readout precision**

98 To verify subnanometer-scale precision of our SpeRe readout, we used a finely tapered glass fiber

99 prepared by thermal drawing of a glass rod using a micropipette puller (**Fig. 2**). In a tapered fiber, the

100 diameter (D) is a smooth function of its longitudinal position (x), therefore we can simply mimic the

101 nanoscale change in diameter (ΔD) by shifting the position (Δx) using a galvanometric scanner. We

102   first estimated the diameter along the fiber using an image acquired by polarization microscopy, and

103   validated by SpeRe (**Fig. 2a-c**). We then selected two points, x_1 and x_2, which showed physiological

104   axon diameters (0.3–5 μm). By the linear regression near the selected points, we acquired the slope

105   (dD/dx), which provided the multiplicative factor for converting the step shift in position (Δx) to the

106   change in diameter (ΔD). For example, to introduce increase in diameter by 0.5 nm at x_2, we shifted

107   the position along the centerline by +55 nm, corresponding to ΔD (0.5 nm) divided by dD/dx (0.009).

108   In a tapered fiber, we obtained broadband reflectance spectra over time on the two selected

109   positions at sampling speed of 20 Hz. To convert the spectral shift (Δν) to the change in physical

110   diameter (ΔD), we applied the linear relationship derived from our numerical simulation for each

111   position (**Supplementary Fig. 2a-c**). The in-position stability of SpeRe acquisition during the initial 2 s

112   was approximately ±0.2 nm at x_1 and ±0.1 nm at x_2 in standard deviation (**Supplementary Fig. 2d-f**).

113   The step shifts in the scan position (Δx) with variable distances were introduced at 2 s after the

114   acquisition (**Fig. 2d-f**). By the step shift in the scan position, we observed the reliable negative

115   spectral shift in wavenumber domain (Δν < 0), corresponding to the swelling. The estimated changes

116   in diameter by SpeRe were precisely matched with the inputs introduced by the shift in position (**Fig.**

117   **2e-f**). These results suggest that our dynamic SpeRe readout provides subnanometer-scale precision.

118

119   **Activity-dependent nanostructural dynamics of myelinated axons**

120   For optical manipulation and recording of neural excitation, we microinjected two types of adeno-

121   associated viruses encoding a red-shifted opsin (AAV9-hSyn-ChrimsonR-tdTomato) and a fluorescent

122   calcium indicator (AAV9-hSyn-GCaMP6s) at the somatosensory cortex of a live mice, and prepared

123   fresh brain slices in oxygenized medium on the experimental day[25,26] (**Fig. 3a**). By combining two-

124   photon fluorescence and confocal reflectance imaging of the brain slice, we could visualize

125   transfected neurons, as well as their myelinated axons. By illuminating 633 nm light pulses following

126   the high frequency stimulation protocol, we observed reliable functional calcium activity in most

127   neuronal soma expressing both ChrimsonR and GCaMP6s[10,13] (**Fig. 3b** and **Supplementary Fig. 3**).

128   To address whether neuronal excitation leads to nanostructural dynamics of myelinated axons,

129   we randomly sampled up to 10 myelinated axons for each brain slice, and recorded the nanoscale

130   dynamics by SpeRe for 5 s with light stimuli ('ChR + Light' group, n = 104 axons in 5 mice; **Fig. 3c,d**).

131   As negative control groups, we included brain slices without light stimuli ('ChR only' group, n = 105

132   axons in 5 mice) and also brain slices without introducing the optogenetic actuator ('Light only' group,

133   n = 105 axons in 5 mice). The SpeRe readout was performed at near the either ends of myelin

134   sheaths, corresponding to the paranode, where axo-myelinic communication is known to be active[27–

135   29]. Apparently, only the group with functional optogenetic excitation ('ChR + Light' group) showed

136   statistically significant spectral shift by ~2,000 cm^{-1} on average (unpaired t-test: $p < 0.05$; **Fig. 3e**).

137   Intriguingly, the spectral shift was cumulatively increased during the 1 s period of optogenetic

138   excitation and slowly recovered in several seconds, indicating that the activity-dependent

139   morphological dynamics does not follow the neuronal membrane potential having millisecond-scale

140   rise and fall kinetics. Moreover, pharmacological inhibition of action potential generation by

141   tetrodotoxin significantly, but only partially, attenuated the swelling, suggesting that the generation of

142   action potentials is not necessary for inducing the swelling (**Supplementary Fig. 4**).

143   To convert the spectral shift (Δv) to the change in physical diameter (ΔD), we applied the linear

144   relationship derived from our numerical simulation (**Supplementary Fig. 1**). As the nanostructural

145   parameters for individual myelinated axons we sampled were not attainable, we applied the

146   representative structural parameters in **Supplementary Table 1** obtained from previous electron

147   micrographs and estimated from our optical images (**Supplementary Fig. 3**)[19,30]. Although this

148   approach compromised the precision of estimation on individual axons, we were able to gain

149   information on the population distribution.

150   Although statistically significant, the group-averaged spectral shift of ~2,000 cm^{-1} corresponds to

151   ~0.2 nm, which was at least several folds smaller than previously reported axonal swelling observed

152   in cell culture and invertebrate systems (**Fig. 3e**). This discrepancy can be explained by our

153   experimental design, which randomly samples myelinated axons in brain slices. Conceivably, a

154   significant portion of long-projecting myelinated axons is expected to be severed during the tissue

155   slicing procedure and contains insufficient optogenetic proteins due to stochastic nature of viral

156   transfection. Consequently, the large portion of the samples even in the 'ChR + Light' group might

157   have been nonresponsive to optogenetic stimuli. Indeed, the histograms of change in diameters for

158   the experimental and the negative control groups were largely similar with statistically significant

159   difference observed only at the swelling greater than ~0.5 nm (**Fig. 3f**).

160   We thus questioned if we could observe reliable nanostructural dynamics in the myelinated

161   axons that are morphologically intact and functionally active (**Fig. 4**). By two-photon imaging of

162   neuronal morphology and functional calcium activity with optogenetic stimuli, we identified the three

163   morphologically intact and functionally active myelinated axons, which were connected to the intact

164   neuronal soma (**Fig. 4a,b**). As expected, the three myelinated axons repeatedly exhibited progressive

165   increase in their diameters by 0.3–1 nm in response to optogenetic stimuli (**Fig. 4c,d** and

166   **Supplementary Fig. 5**). We further observed that the morphological dynamics was localized to the

167   paranode (**Fig. 4e**) and that the degree of swelling was positively correlated with the duration of

168   optogenetic stimuli (**Fig. 4f**).

169

170

171   **DISCUSSION**

172

173   By combining nanoscale readout based on spectral interferometry (SpeRe) and optogenetic

174   manipulation of neural excitation, we reported the first experimental evidence that myelinated axons

175   exhibit activity-dependent subnanometer-scale morphological dynamics of ~0.5 nm. We further

176   revealed that the nanostructural change displays slow kinetics at second-scale and localized to the

177   paranode. As conduction efficacy of neural information has steep dependence on the subcellular

178   structure of the paranode, we expect that its nanostructural dynamics can serve as a regulatory mode

179   of controlling conduction speed in the mammalian brains.

180   The functional consequence of the morphological remodeling at the paranode can be inferred

181   by the periaxonal nanocircuit model of the myelinated axons[10]. According to this model, the periaxonal

182   space is electrically conductive and the paranodes are only partially sealed, resulting in leaky

183   propagation of neural information. Thus, the swelling of the paranode can attenuate the leakage and

184   accelerate the conduction speed. By the theoretical double cable model, 1 nm swelling at the

185   paranode leads to ~1.3% acceleration in conduction speed. Accordingly, the observed swelling of ~0.5

186   nm is expected to increase the conduction speed by ~0.7%. Consistently, Yamazaki et al. reported

187   short-term increase in conduction speed by directly depolarizing the myelinating oligodendrocyte[28,31].

188   The physiological relevance of this change in conduction velocity on neural circuit function requires

189   further investigation.

190   Our results revealed that the paranodal swelling occurs cumulatively and reversibly at second

191   scale, suggesting that the neuronal membrane potential having millisecond-scale rise and fall kinetics

192   is not the direct source of the swelling (**Fig. 3d** and **Fig. 4d**). In addition, pharmacologic inhibition of

193   voltage-gated sodium channel by tetrodotoxin only partially attenuated the paranodal swelling

194   (**Supplementary Fig. 4**), suggesting that generation of action potential is not necessary for inducing

195   the swelling. Considering that ChrimsonR is light-gated channel permeable to both sodium and

196   calcium ions[26,32], we expect the calcium influx may play a key role in the paranodal swelling. In

197   agreement with our thought, we observed calcium transients by ChrinsonR-mediated optogenetics in

198   our inhibition study with tetrodotoxin, and the degree of calcium increase was attenuated compared to

199   the control group. Further pharmacological inhibition of ion channel subtypes or use of ion-selective

200   opsins will clarify the underlying molecular mechanism.

201   Although our results consistently suggest that the neuronal excitation leads to enlargement of

202   myelinated axons at the paranode, it remains to be answered which subcellular components are

203   remodeled. Chéreau et al. reported that high frequency stimulation of neurons leads to axonal

204   swelling in the mouse brain[15]. Trigo and Smith also showed that micron-scale axonal swelling

205   following prolonged electric stimulation of the peripheral nerves[27]. As mature myelin sheaths do not

206   typically exhibit axonal activity dependent functional responses, we estimate that the axon at the node

207   of Ranvier swells in response to ionic redistribution across the membrane and the surrounding myelin

208   is passively enlarged. Detailed multiparametric analysis based on the thin-film model with a priori

209   structural information on each subcellular composition may provide a solution to this question.

210

211

METHODS

Tapered glass fiber sample: The tapered glass fibers were obtained by the thermal drawing of a glass rod (1.5 mm in diameter) using a micropipette puller (P-1000, Sutter Instrument). To mimic the typical axon diameters (1–5 µm), the optimal parameters for the micropipette puller were obtained by trials and errors (ramp = 500 temperature = 550, pull = 40, velocity = 20, and pressure = 500). The tapered fiber was glued on a plain slide glass using an acrylic adhesive (401, Loctite) ensuring that the fiber is parallel to the slide glass (i.e., orthogonal to the optical axis of the objective lens). To firmly hold the fiber, a silicone-based sealant (Kwik-Cast, World Precision Instruments) was introduced around the fiber tip, exposing only the fiber tip in the air. The sample was imaged by a polarization microscope (SP8, Leica) and the diameter along the fiber was measured by applying the 'Distance map' module in ImageJ.

Artificial cerebrospinal fluid (aCSF): Two types of artificial cerebrospinal fluid (aCSF) solutions were prepared, one is for surgery and the other is for recording. The surgical aCSF was composed of (in mM) 92 NMDG, 2.5 KCl, 1.25 NaH_2PO_4, 30 $NaHCO_3$, 20 HEPES, 25 glucose, 2 thiourea, 5 Na-ascorbate, 3 Na-pyruvate, 0.5 $CaCl_2 \cdot 2H_2O$, and 10 $MgSO_4 \cdot 7H_2O$. The recording aCSF was composed of (in mM) 124 NaCl, 2.5 KCl, 1.2 NaH_2PO_4, 24 $NaHCO_3$, 12.5 glucose, 2 $CaCl_2 \cdot 2H_2O$, and 2 $MgSO_4 \cdot 7H_2O$ (Sigma Aldrich). Both solutions were titrated to have pH 7.3–7.4 and 300–310 mOsm while aerated with 95% O_2 and 5% CO_2.

Mouse preparation: All mice were housed with littermates in groups of two to five in reverse day/night cycle and given ad libitum access to food and water. All animal experiments were performed in compliance with institutional guidelines and approved by the sub-committee on research animal care at Sungkyunkwan University and Seoul National University. Male or female C57BL6J wild-type mice aged 4-week-old (Jackson Laboratory) were used for virus-mediated transduction of a genetically-encoded calcium indicator (GCaMP6s) and/or an optogenetic protein (ChrimsonR-tdT). The mouse was anesthetized by inhaling 4% isoflurane (Hanapharm) in an induction chamber and were subsequently maintained with 1–1.5% isoflurane during surgery. The mouse skull was affixed on a custom-made stereotaxic frame and the body temperature was maintained at 37°C using a homeothermic blanket (TC-1000, CWE) and a thermistor probe (YSI-451, CWE). After removing the scalp, the hole was made on the center of the somatosensory area at a diameter of ~1 mm. The 700 nL of a solution containing AAV9- hSyn-GCaMP6s and/or AAV5-hSyn-Chrimson-tdTomato (~5 x 10^{11} GC·ml^{-1} each in the recording aCSF) was slowly infused to the cortical layer 3–4. After 3 weeks, the mice were used for the acute slice experiments.

Kwon et al., 2022

249

250   **Brain slice preparation:** Mice were decapitated under deep anesthesia by inhaling 3%

251   isoflurane in O_2. The mouse brain was harvested and sliced using a vibratome (thickness =

252   300 µm; VT1200S, Leica). During the slicing procedure, the immersion solution was the

253   surgical aCSF solution kept at 4°C. Subsequently, the brain slices were incubated in the

254   surgical aCSF solution at 35°C for 20 min and were immersed in the recording aCSF

255   solution at room temperature (22–24°C) with continuous aeration of 95% O_2 and 5% CO_2 for

256   30min. The brain slices were mounted on an imaging chamber using a tissue anchor (SHD-

257   41/10, Warner instruments). For the neuronal inhibition study, tetrodotoxin (TTX) was added

258   to the recording aCSF at 10 µM.

259

260   **Optic setup**: Our customized optic system shown in Fig. 1b was designed to incorporate the

261   following 3 modalities: (i) two-photon fluorescence imaging for recording neuronal activity; (ii)

262   spectral reflectance spectroscopy for nanostructural readout of myelinated axons; and (iii)

263   optogenetics for manipulating neural activity. The system was constructed based on an

264   upright galvanometer-based laser scanning microscope (Ultima IntraVital, Bruker), coupled

265   to a Ti-Sapphire femtosecond laser (for two-photon fluorescence imaging; Chameleon Ultra

266   II, Coherent) and a supercontinuum white-light laser (for SpeRe and SCoRe; EXB-6, NKT

267   photonics). The femtosecond laser was tuned to 920 nm for exciting GCaMP6s and was

268   attenuated to 10–20 mW at the objective back aperture. The supercontinuum laser was

269   attenuated to ~0.4 mW at the objective back aperture using a neutral density filter and

270   bandpass-filtered to 450–700 nm. An apochromatic water-immersion objective lens (25X,

271   0.95 NA, Leica) was used for both two-photon fluorescence and SpeRe/SCoRe readouts.

272   For two-photon fluorescence imaging, a GaAsP photomultiplier tube placed at the non-

273   descanned path was used along with a bandpass filter at 500–550 nm. For the SCoRe

274   imaging, a silicon photomultiplier tube placed at the descanned path was used. For SpeRe

275   measurements, an array spectrometer (SR303i and Newton, Andor) was introduced at the

276   descanned path. For spectroscopy, the grating of 600 lines·mm^{-1} was adjusted to accept

277   spectral window of 550 to 650 nm, where the input white light exhibited near uniform

278   intensity profile over the spectral window. The slit size was set to 10 µm, providing a spectral

279   resolution ~0.13 nm with enough signal-to-noise ratio at acquisition speed of 20 Hz. For

280   optogenetics, a 633 nm diode laser (MRL-III-633, CNI laser) was coupled to a multimode

281   fiber (400 µm core, 0.39 NA; M119L02, Thorlabs), which was mounted on a motorized 3-axis

282   micromanipulator (MP-285, Sutter Instrument). Optical irradiance for optogenetic stimulation

283   was set to 10 mW·mm^{-2} at the tissue surface, which was delivered at 100 Hz with 50% duty

284   cycle for the duration of 0.5–2 s.

9

285

286   **Data analysis**: For SpeRe, the time-series reflectance spectrums were filtered in spectral

287   and time domains in Matlab. To reduce artifactual jittering noise, the lowpass filter at a cutoff

288   frequency of 0.65 nm^{-1} was applied in the wavelength domain by applying the 'lowpass'

289   function, and the smoothing filter with the bin of 0.5 s was applied in temporal domain by

290   using the 'smooth data' function. From the filtered spectral data, relative phase shift over

291   time from the baseline was retrieved based on the least-square method. Occasionally,

292   unpredictable motion artifacts (e.g., instability of media perfusion) interfered reliable

293   quantification of the phase shift. Thus, we excluded the data if it displayed at least one of the

294   following indications of excessive motion artifact: change in reflectance intensity greater than

295   10% and the phase drifted over 3 nm. For calcium imaging data, we quantified relative

296   change in fluorescence normalized by the baseline fluorescent intensity (ΔF/F).

297

298   **Statistical analysis:** GraphPad Prism was used for statistical analysis. Group comparisons were

299   conduction using unpaired t-tests (parametric). The data are presented as mean ± standard error. We

300   considered a p-value less than 0.05 to be statistically significant.

301

302   **Code availability:** The MATLAB scripts used for data analysis are available at an open source

303   repository (https://github.com/Neurophoton).

304

305   **Data availability:** All relevant data are available from the corresponding author upon request. A

306   reporting summary for this Article is available as a Supplementary Information file.

307   **References**

308   1.   Akkin, T., Landowne, D. & Sivaprakasam, A. Optical coherence tomography phase
309   measurement of transient changes in squid giant axons during activity. *J. Membr. Biol.* **231**, 35–
310   46 (2009).

311   2.   Yang, Y. *et al.* Imaging action potential in single mammalian neurons by tracking the
312   accompanying sub-nanometer mechanical motion. *ACS Nano* **12**, 4186–4193 (2018).

313   3.   Tang, J. *et al.* Imaging localized fast optical signals of neural activation with optical coherence
314   tomography in awake mice. *Opt. Lett.* **46**, 1744–1747 (2021).

315   4.   Hill, B. C., Schubert, E. D., Nokes, M. A. & Michelson, R. P. Laser interferometer measurement
316   of changes in crayfish axon diameter concurrent with action potential. *Science (80-.).* **196**, 426–
317   428 (1977).

318   5.   Iwasa, K., Tasaki, I. & Gibbons, R. C. Swelling of nerve fibers associated with action potentials.
319   *Science (80-.).* **210**, 338–339 (1980).

320   6.   LaPorta, A. & Kleinfeld, D. Interferometric detection of action potentials. *Cold Spring Harb.*
321   *Protoc.* **2012**, pdb-ip068148 (2012).

322   7.   Andersen, S. S. L., Jackson, A. D. & Heimburg, T. Towards a thermodynamic theory of nerve
323   pulse propagation. *Prog. Neurobiol.* **88**, 104–113 (2009).

324   8.   Stepnoski, R. A. *et al.* Noninvasive detection of changes in membrane potential in cultured
325   neurons by light scattering. *Proc. Natl. Acad. Sci.* **88**, 9382–9386 (1991).

326   9.   Richardson, A. G., McIntyre, C. C. & Grill, W. M. Modelling the effects of electric fields on nerve
327   fibres: influence of the myelin sheath. *Med. Biol. Eng. Comput.* **38**, 438–446 (2000).

328   10. Cohen, C. C. H. *et al.* Saltatory conduction along myelinated axons involves a periaxonal
329   nanocircuit. *Cell* **180**, 311–322 (2020).

330   11. Cullen, C. L. *et al.* Periaxonal and nodal plasticities modulate action potential conduction in the
331   adult mouse brain. *Cell Rep.* **34**, 108641 (2021).

332   12. Hughes, E. G., Orthmann-Murphy, J. L., Langseth, A. J. & Bergles, D. E. Myelin remodeling
333   through experience-dependent oligodendrogenesis in the adult somatosensory cortex. *Nat.*
334   *Neurosci.* **21**, 696–706 (2018).

335   13. Gibson, E. M. *et al.* Neuronal Activity Promotes Oligodendrogenesis and Adaptive Myelination in
336   the Mammalian Brain. *Science (80-.).* **344**, 1252304 (2014).

337   14. Stedehouder, J., Brizee, D., Shpak, G. & Kushner, S. A. Activity-dependent myelination of
338   parvalbumin interneurons mediated by axonal morphological plasticity. *J. Neurosci.* **38**, 3631–
339   3642 (2018).

340   15. Chéreau, R., Saraceno, G. E., Angibaud, J., Cattaert, D. & Nägerl, U. V. Superresolution
341   imaging reveals activity-dependent plasticity of axon morphology linked to changes in action
342   potential conduction velocity. *Proc. Natl. Acad. Sci.* **114**, 1401–1406 (2017).

343   16. D'Este, E., Kamin, D., Balzarotti, F. & Hell, S. W. Ultrastructural anatomy of nodes of Ranvier in
344   the peripheral nervous system as revealed by STED microscopy. *Proc. Natl. Acad. Sci.* **114**,
345   E191–E199 (2017).

346   17. Tillberg, P. W. *et al.* Protein-retention expansion microscopy of cells and tissues labeled using

11

347   standard fluorescent proteins and antibodies. *Nat. Biotechnol.* **34**, 987–992 (2016).

348   18. Young, K. M. *et al.* Oligodendrocyte dynamics in the healthy adult CNS: Evidence for myelin

349   remodeling. *Neuron* **77**, 873–885 (2013).

350   19. Kwon, J. *et al.* Label-free nanoscale optical metrology on myelinated axons in vivo. *Nat.*

351   *Commun.* **8**, 1–9 (2017).

352   20. Emiliani, V., Cohen, A. E., Deisseroth, K. & Häusser, M. All-optical interrogation of neural

353   circuits. *J. Neurosci.* **35**, 13917–13926 (2015).

354   21. Schain, A. J., Hill, R. A. & Grutzendler, J. Label-free in vivo imaging of myelinated axons in

355   health and disease with spectral confocal reflectance microscopy. *Nat. Med.* **20**, 443–449

356   (2014).

357   22. Debnath, S. K., Kothiyal, M. P., Schmit, J. & Hariharan, P. Spectrally resolved white-light phase-

358   shifting interference microscopy for thickness-profile measurements of transparent thin film

359   layers on patterned substrates. *Opt. Express* **14**, 4662–4667 (2006).

360   23. Kim, D. & Kim, S. Direct spectral phase function calculation for dispersive interferometric

361   thickness profilometry. *Opt. Express* **12**, 5117–5124 (2004).

362   24. Sandoz, P., Tribillon, G. & Perrin, H. High-resolution profilometry by using phase calculation

363   algorithms for spectroscopic analysis of white-light interferograms. *J. Mod. Opt.* **43**, 701–708

364   (1996).

365   25. Chen, T.-W. *et al.* Ultrasensitive fluorescent proteins for imaging neuronal activity. *Nature* **499**,

366   295–300 (2013).

367   26. Klapoetke, N. C. *et al.* Independent optical excitation of distinct neural populations. *Nat.*

368   *Methods* **11**, 338–346 (2014).

369   27. Trigo, D. & Smith, K. J. Axonal morphological changes following impulse activity in mouse

370   peripheral nerve in vivo: the return pathway for sodium ions. *J. Physiol.* **593**, 987–1002 (2015).

371   28. Yamazaki, Y. *et al.* Modulatory effects of oligodendrocytes on the conduction velocity of action

372   potentials along axons in the alveus of the rat hippocampal CA1 region. *Neuron Glia Biol.* **3**, 325

373   (2007).

374   29. Micu, I. *et al.* The molecular physiology of the axo-myelinic synapse. *Exp. Neurol.* **276**, 41–50

375   (2016).

376   30. Jarjour, A. A. *et al.* Maintenance of axo-oligodendroglial paranodal junctions requires DCC and

377   netrin-1. *J. Neurosci.* **28**, 11003–11014 (2008).

378   31. Yamazaki, Y. *et al.* Region-and cell type-specific facilitation of synaptic function at destination

379   synapses induced by oligodendrocyte depolarization. *J. Neurosci.* **39**, 4036–4050 (2019).

380   32. Mager, T. *et al.* High frequency neural spiking and auditory signaling by ultrafast red-shifted

381   optogenetics. *Nat. Commun.* **9**, 1–14 (2018).

382

Acknowledgments

Author contributions

M.C. initiated and supervised the study. Y.J. developed the optical hardware and acquisition software. J.K. performed the brain slice experiments and data analysis. All the authors cowrote the manuscript.

Competing interests

The authors declare no competing interests.

Corresponding author

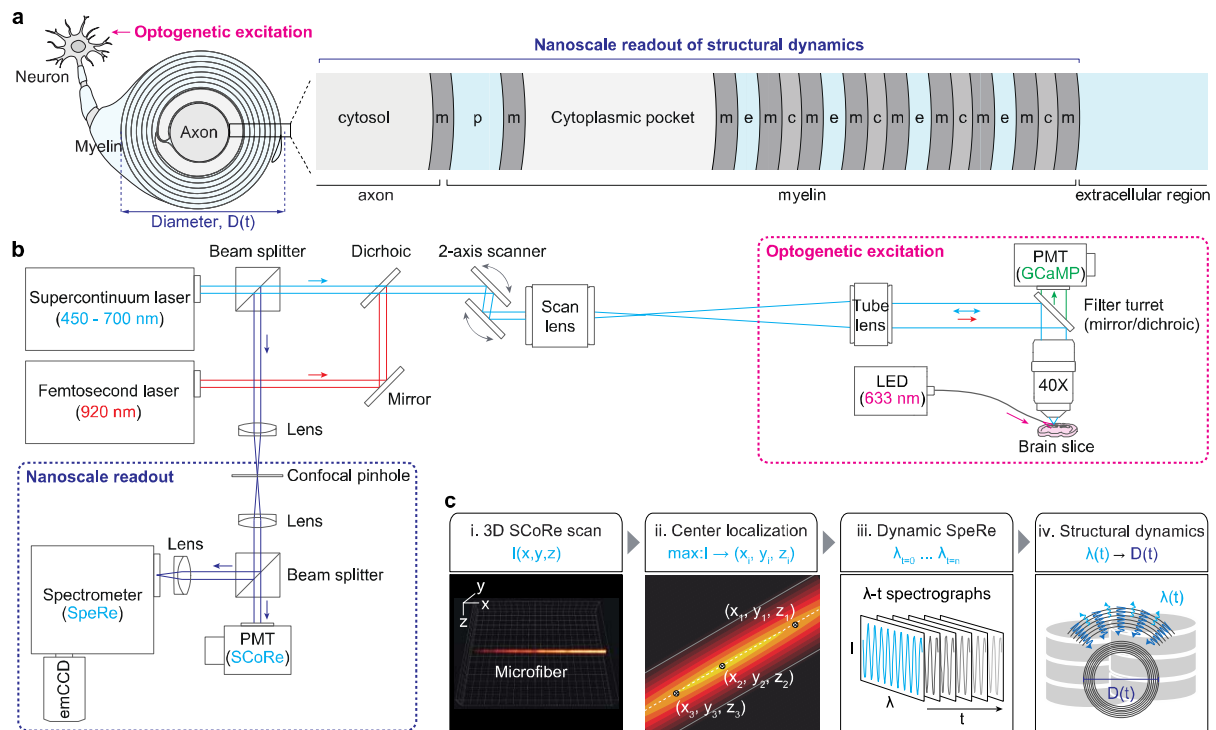Correspondence to M. Choi (e-mail: choim@snu.ac.kr)

Figure 1

Figure 1 | All-optical approach for observing activity-dependent nanostructural dynamics of living myelinated axons. (**a**) A cross-sectional view on the nanoscale cytoarchitecture of a myelinated axon at the paranodal region. The thin-film layers of the myelinated axons are shown in the magnified view. m, membrane. p, periaxonal space. c, cytosolic layer of the myelin. e, extracellular region. D, diameter. t, time. (**b**) The optic setup incorporating spectral confocal reflectance imaging (SCoRe), spectral reflectometry (SpeRe), two-photon fluorescence imaging, and optogenetic excitation. The supercontinuum laser serves as a light source for SpeRe and SCoRe, and the femtosecond laser provides two-photon excitation for recording GCaMP-mediated neuronal calcium activity. The auxiliary fiber-coupled light-emitting diode (LED) at 633 nm was used for triggering ChrimsonR-mediated excitatory optogenetics. (**c**) A pipeline for the nanoscale readout of structural dynamics of a myelinated axon. i, 3D SCoRe scan to acquire a volumetric reflectance image of myelinated axons. ii, Localization of the geometric centers based on the maximal reflectance intensity. iii, Time-lapse acquisition of the reflectance spectrographs at the geometric center. iv. Decoding of the structural dynamics from the acquired spectrographs. I, intensity. λ, wavelength.
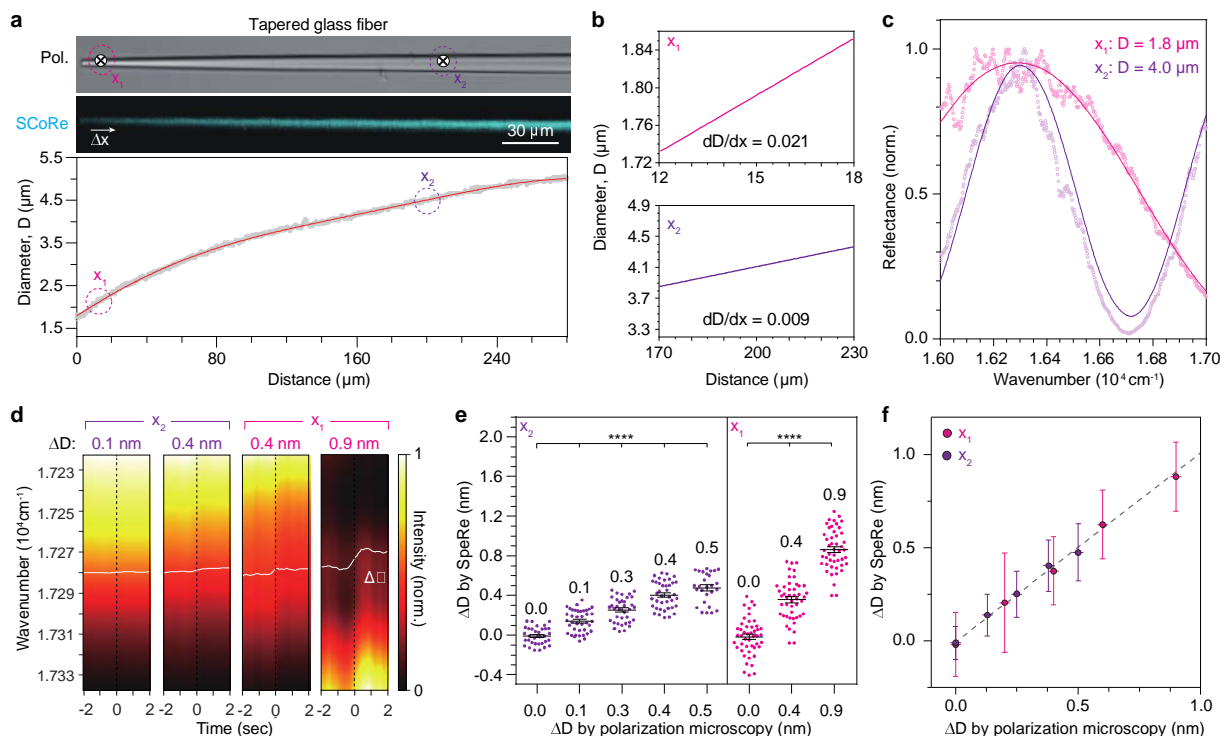
Figure 2

Figure 2 | Validation on nanometer-scale readout precision of SpeRe. (**a**) A tapered glass fiber sample for quantifying the nanoscale readout precision. The tapered fiber is imaged by polarization microscopy (Pol.) and spectral confocal reflectance imaging (SCoRe). The gradually varying diameter (D) along the fiber was acquired from the polarization microscopic image. (**b**) The spatial derivatives of the diameter (dD/dx) at the representative positions (x_1 and x_2) along the tapered glass fiber. (**c**) Reflectance spectrographs at the positions, x_1 and x_2. The acquired spectrographs (dots) were overlaid with best-fit simulated spectrums (curved lines). (**d**) Representative time-lapse reflectance spectrographs measured at the indicated positions (x_1 for $\Delta D = 0.4$ nm and 0.9 nm; x_2 for $\Delta D = 0.1$ nm and 0.4 nm) with step shifts in position at 0 s. The step change in position was introduced by shifting the focal point along the centerline of the fiber. The white curves indicate the relative spectral shift. (**e-f**) Change in diameters (ΔD) estimated by SpeRe with the corresponding estimates by polarization microscopy. *, $p < 0.0001$ (unpaired t-test). The error bars indicate standard deviations.
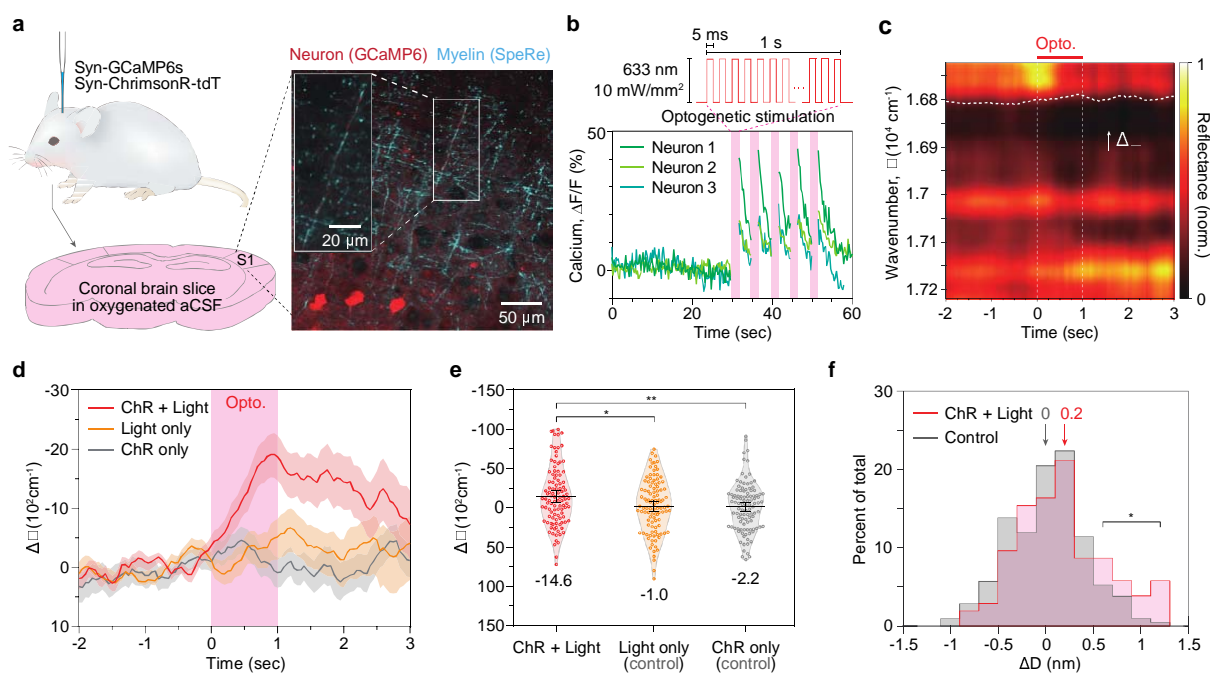
Figure 3

Figure 3 | All-optical observation of activity-dependent subnanometer-scale swelling of myelinated axons. (**a**) Sample preparation. The neurons in the somatosensory cortex (S1) were transfected with a fluorescent calcium indicator (GCaMP6s) and an optogenetic actuator (ChrimsonR). A representative fluorescence/reflectance image from the brain slice is shown on the right. (**b**) Optogenetic excitation. Neurons transfected with ChrimsonR was excited by illuminating pulsed light (wavelength: 633 nm, irradiance: 10 mW/mm^2, frequency: 100 Hz, pulse width: 5 ms). Calcium traces in soma from 3 neurons in (a) are shown. The shaded areas in pink indicate the duration of optogenetic stimulation. (**c**) A representative phase shifts (Δ□) induced by the optogenetic neural activity. The red bar indicates the duration of optogenetic stimulus (1 s). The white dashed line indicates the relative phase shift from the baseline (-1.0 – -0.5 s). (**d**) The group averaged phase shifts (Δ□) for each experimental group. The red curve ('ChR + Light' group, n = 104 axons in 5 mice) indicates the ChrimsonR-expressing neurons with light stimulus, the yellow curve ('Light only' group, n = 105 axons in 5 mice) indicates the wild-type neurons receiving photostimulation, and the gray curve ('ChR only' group, n = 105 axons in 5 mice) indicates the ChrimsonR-expressing neurons without light stimulus. Note that only the 'ChR + Light' group exhibited distinguishable negative shift in wavenumber. (**e**) Statistical group comparison of phase-shifts (Δ□) in (d). The phase-shifts were quantified by averaging the relative phase shifts during 0.5–1 s. *, p < 0.05 (unpaired t-test). **, p < 0.01 (unpaired t-test). (**f**) Histograms of activity-dependent changes in diameters of myelinated axons (ΔD). The positive value of ΔD corresponds to swelling.
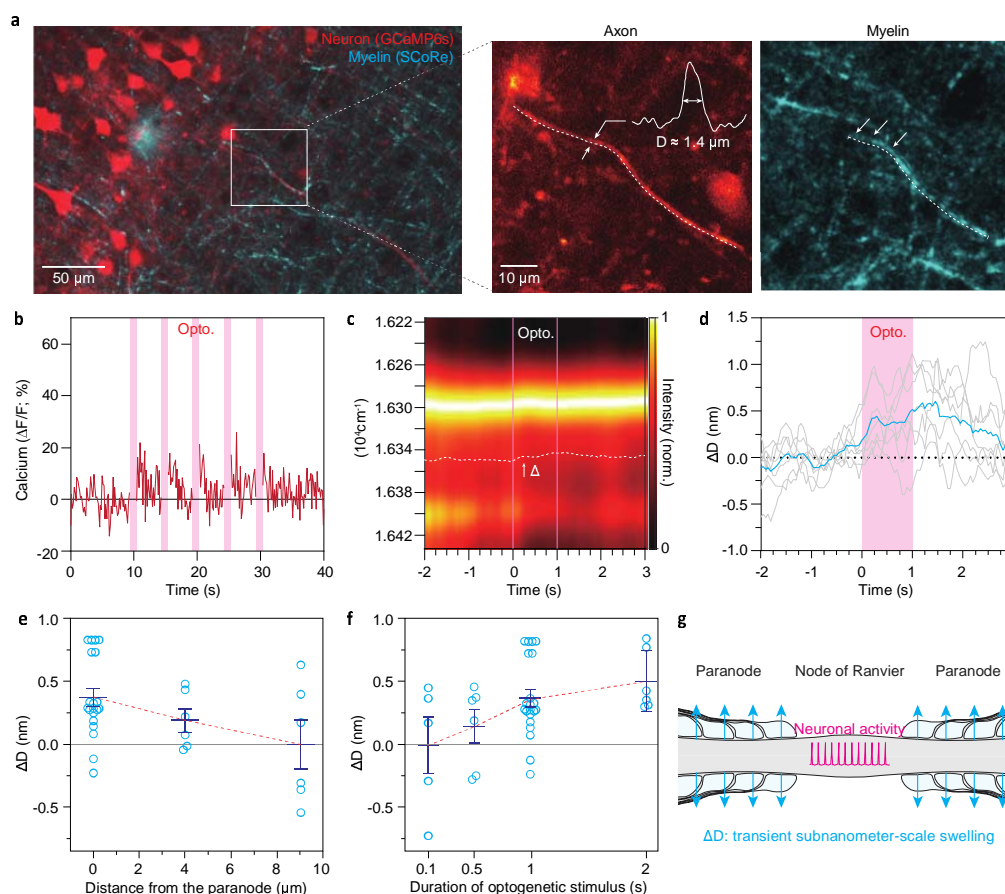
Figure 4

Figure 4 | Correlative characterization of subnanometer-scale swelling in an optogenetically active axon. (a) Representative images of myelinated axons. The neurons are imaged by two-photon fluorescence of GCaMP6s (red) and the myelin is visualized by SCoRe (cyan). The magnified view of the myelinated axon of interest is shown on the left. The axon diameter (D) was estimated to by full-width-half-maximum of the transverse intensity profile (D ≈ 1.4 μm). The dashed lines indicate the axon and the myelin sheath. **(b)** Axonal calcium activity triggered by optogenetic excitation of ChrimsonR. The shaded area in magenta indicates the duration of optogenetic excitation (633 nm, 10 mW/mm^2). **(c)** Observation of time-dependent change in reflectance spectrum at the optogenetically active myelinated axon. The dashed lines indicate the duration of optogenetic stimulation. Note the progressive spectral redshift (Δ□) during the optogenetic stimulation. **(d)** Time dependent changes in the diameter of myelinated axons (ΔD) in response to optogenetic stimulation (shaded region in magenta). Cyan curve indicates the averaged trace of 7 repeated trials (individual traces are shown in grey). **(e)** The swelling is localized to the paranode. **(f)** Dependency of ΔD on the duration of optogenetic stimuli at the paranode. (**g**) The schematic diagram of the activity-dependent nanoscale dynamics of the myelinated axons.